




Kinetics of Reverted Austenite in 18 wt.% Ni Grade 300 Maraging Steel: An In-Situ Synchrotron X-Ray Diffraction and Texture Study

LUIS PAULO MOURÃO DOS SANTOS ^{1,7} MILOSLAV BÉREŠ^{1,2}
MIRELA OLIVEIRA DE CASTRO,¹
PAULO WILLIAN CARVALHO SARVEZUK,³ LEONARDO WU,⁴
LUIS FLÁVIO GASPAR HERCULANO,¹ ANDREA PAESANO JR.,⁵
CLEITON CARVALHO SILVA,¹ MOHAMMAD MASOUMI,⁶
and HAMILTON FERREIRA GOMES DE ABREU¹

1.—Department of Metallurgical and Materials Engineering, Federal University of Ceará, Campus do Pici, Av. Humberto Monte, Fortaleza, CE 60445-554, Brazil. 2.—BIOFABRIS - National Institute of Science and Technology in Biomanufacturing, Faculty of Chemical Engineering, University of Campinas, Av. Albert Einstein 500, Campinas, SP 13081-970, Brazil. 3.—Department of Physics, Federal Technological University of Paraná, Via Rosalina Maria dos Santos, Campo Mourão, PR 87301-899, Brazil. 4.—Brazilian Center for Research in Energy and Materials - CNPEM, R. Giuseppe Máximo Solfaro 10000, Campinas, SP 13083-970, Brazil. 5.—Department of Physics, State University of Maringá, Av. Colombo 5790, Maringá, PR 87020-900, Brazil. 6.—Center of Engineering, Modelling and Applied Social Sciences, Federal University of ABC, Av. dos Estados, 5001, Santo André, SP 09210-580, Brazil. 7.—e-mail: santoslp@metalmat.ufc.br

In this study, we investigated the transformation kinetics of martensite \rightarrow reverted austenite in 18 wt.% grade 300 Ni maraging steel. The kinetics was evaluated based on the in situ synchrotron x-ray diffraction data collected during isothermal heat treatment at 570°C. The onset of transformation martensite \rightarrow reverted austenite was detected after \sim 5 min of aging. The austenite fraction increased as a function of annealing time and reached approximately 30 vol.% after 3 h of heat treatment. The electron backscatter diffraction technique revealed that reverted austenite is formed preferentially on both the martensitic lath boundaries and sub-grain boundaries inside the laths, in particular in those with high Taylor factor values. The reverted austenite maintains an orientation relationship with the prior austenite; however, variant selection can take place.

INTRODUCTION

Precipitation-hardened martensitic high-strength maraging steels are primarily employed in aircraft, aerospace, tooling and power generation applications.^{1–4} After hot working, the steel is usually solution annealed at a temperature $>$ 800°C followed by cooling to room temperature to produce a soft martensitic matrix. Then, the material is subjected to aging heat treatment typically at 480°C, which leads to precipitation of fine dispersed particles. Various types of precipitates, such as Ni₃Mo, Ni₃Ti, Fe₂Mo and Fe₂Ti, can precipitate during the aging.¹ During the early stages of aging

treatment, mainly Ni₃(Ti,Mo) and Fe₇Mo₆ are formed.^{2–4} If the steel is aged at higher temperatures of \sim 550°C (below A_{c1} temperature) or for prolonged times, an austenite reversion can be induced by a partial transformation from martensite.^{5,6} This is a diffusion-controlled process of segregation of austenite stabilizer elements into martensitic lath boundaries.^{7,8} The reverted austenite can nucleate and grow within the martensitic laths in the form of twins. This kind of austenite is termed intra-lath reverted austenite.⁹ Another possibility for reverted austenite formation is along the interfaces. The interfaces include prior austenite

grain boundaries in addition to martensite packets, blocks and lath boundaries.^{10,11} This austenite is usually called inter-lath reverted austenite.

It is important to distinguish between reverted austenite and retained austenite since the latter is the result of incomplete transformation of austenite to martensite during cooling from solution annealing temperature.^{12,13}

Several studies have been conducted to correlate the formation of reverted austenite to the mechanical behavior of maraging steels.^{14–16} The authors of Refs.^{6,17} argued that the formation of reverted austenite is accompanied by a coarsening of the strengthening precipitates, which results in a rapid loss of strength. In contrast, other studies have reported that steels containing reverted nanoscale austenite islands or films dispersed in a martensitic matrix exhibited an excellent combination of strength, ductility and toughness.^{18–20} Pampillo et al.²¹ claimed that the introduction of reverted austenite on martensite lath boundaries did not reduce the yield stress of the 18 wt.% Ni maraging steel because of the severity of transmitting slip across these boundaries.

The presence of reverted austenite in maraging steels is commonly determined by x-ray diffraction,^{22,23} the eddy current method^{24,25} and small-scale (nm, μm) microstructural techniques including transmission electron microscopy (TEM),^{9,22,26,27} Mössbauer spectroscopy²⁸ and atom probe tomography (APT).^{7,8} The electron backscatter diffraction (EBSD) technique can also be employed to study the formation of reverted austenite in maraging steel. This technique allows analysis of large-scale areas (up to several cm) where the crystal structure, texture, grain boundary characteristics, phase transformation and orientation relationship between phases in many grains can be followed.

The orientation relationship between reverted austenite and martensite has been reported to be close to that of Kurdjumov–Sachs (KS) or Nishiyama–Wassermann (NW).^{29,30} Nakada et al.³¹ employed the EBSD technique and found that in 13%Cr-6%Ni low-carbon martensitic steel most of the reverted austenite grains maintain the identical crystallographic orientation as the prior austenite. However, in some reverted austenite grains a twin orientation close to the KS relationship was identified. This was attributed to the presence of internal stress introduced by martensitic transformation.

Despite numerous studies conducted on the formation of reverted austenite in 18 wt.% Ni maraging steels,^{21,23,27,28,32} there is still a discrepancy among different reports. We believe this is due to the experimental procedure and/or sample preparation usually used by the researchers. For example, examining 18 wt.% Ni maraging steel by conventional x-ray diffraction, Pardal et al.²³ reported reverted austenite values of 26.3 vol.% after aging at 560°C for 10 h, while Pampillo and Paxton²¹ obtained around 35 vol.% reverted austenite after

aging at 565°C for 3 h. Furthermore, Nunes et al.²⁸ conducted heat treatment at 580°C for 3 h and determined around 8.5 vol.% reverted austenite, whereas Markfeld and Rosen³² observed approximately 30 vol.% reverted austenite in 18 wt.% Ni maraging steel subjected to an identical heat treatment. Notably, in the mentioned studies, the transformation kinetics was analyzed *post mortem* after the heat treatment was performed and the sample cooled down. Therefore, this approach does not allow assessing the thermal stability of reverted austenite during cooling from the annealing temperature. In addition, it is reported that the reverted austenite can transform to martensite by application of an external load.^{18,33,34} Therefore, the mechanical polishing of the heat-treated material prior to conventional XRD and/or microstructural analysis could lead to ambiguous results due to the deformation-induced transformation.³⁵ Recently, phase transformation was studied in situ using neutron or x-ray diffraction with high-energy synchrotron radiation.^{36–48} This time-resolved approach allows monitoring features of phase transformation as a function of applied load, temperature, cooling and heating rate. Conde et al.⁴⁸ used a time-resolved synchrotron x-ray diffraction technique to study the martensite \rightarrow reverted austenite process in selectively laser sintered 18 wt.% Ni maraging steel. They demonstrated that isothermal heat treatment up to 650°C produced reverted austenite with high thermal stability during cooling to room temperature.

Wang et al.¹⁸ investigated the effect of size on reverted nanoscale austenite transformation in a model TRIP-maraging steel. The authors claimed an unexpected “smaller is less stable” effect due to the size-dependent competition between mechanical twinning and deformation-induced phase transformation. In addition, the partitioning and chemical gradients of alloying elements across phase boundaries between martensite and austenite were studied experimentally and using a thermodynamic approach.^{7,8,49–51}

In this work, we examine the kinetics of reverted austenite in 18 wt.% grade 300 Ni maraging steel by analysis of time-resolved synchrotron x-ray diffraction data collected during isothermal heat treatment at 570°C. This approach allowed us to follow the transformation kinetics without the need for additional sample preparation, which can be a critical issue in samples susceptible to deformation-induced martensitic transformation. Using EBSD analysis, we determined the orientation relationship between reverted austenite and the prior austenite. In addition, we found that reverted austenite nucleates at martensitic lath boundaries with high Taylor factor values. To the authors’ knowledge, none of the published papers examine the effect of Taylor factor values on the nucleation and growth of reverted austenite in maraging

steels. By coupling various experimental techniques and applying computational simulation of solid-state transformation, this study aims to fill this gap.

EXPERIMENTAL

The studied material was grade 300 commercial maraging steel containing 18.7 Ni, 9.6 Co, 4.8 Mo, 0.9 Ti and 0004 C balance Fe (wt.%) supplied by a Brazilian steel company. Tensile test samples with $4 \times 2 \text{ mm}^2$ cross-section and 4 mm gauge length were machined from a 10-mm-thick disk cut from a 300-mm-diameter forged bar. Prior to the machining, the disk was subjected to solution annealing at 840°C for 1 h followed by air cooling to ambient temperature. The sample gauge length was electropolished using a solution consisting of 5 vol.% perchloric acid in ethanol at 19 V. Then, the tensile sample was mounted in a Gleeble thermomechanical simulator integrated within the XTMS beamline at the Brazilian Synchrotron Light Laboratory, Campinas, Brazil. In-situ isothermal heat treatment at 570°C for 3 h applying a heating rate of 15°C s^{-1} was conducted using direct current heating under simultaneous acquisition of one-dimensional diffraction patterns. The temperature of the sample was controlled using R-type thermocouples welded in the center of the specimen. A monochromatic x-ray beam with dimensions of the slit system of $2.0 \times 0.5 \text{ mm}^2$ and wavelength of 1.0332 Å (12 keV) was used to illuminate the sample, which was tilted 15° relative to the incident x-ray beam. The diffraction patterns were acquired using two silicon microstrips MYTHEN one-dimensional linear detectors. During the heat treatment, diffraction patterns in the 2θ range of 28° – 43° were collected every 10 s. These scans are named partial scans. A complete scan in the range of $2\theta = 25^\circ$ – 81° was acquired prior to the test and then every 20 min of the heat treatment. The instrument parameters were obtained using Al_2O_3 powder standard.

The measured data consisted of a series of diffraction patterns as function of time.

The diffraction patterns were refined by the Rietveld method^{52,53} using the FullProf program⁵⁴ considering the $I4$ and $Fm - 3m$ space groups attributed to the martensite and austenite phase, respectively. The phase volume fraction was determined from the weight fraction calculated by:⁵⁵

$$W_j = \left(\frac{s_j Z_j M_j V_j}{\sum s_i Z_i M_i V_i} \right) \quad (1)$$

where i and j represent each phase and s is the scale factor, Z the number of formula units per unit cell, M is the mass per formula unit and V the unit cell volume.

A Philips Panalytical® texture goniometer was used to measure three incomplete pole figures {200}, {110}, and {211} of the bcc-martensite and {111}, {200} and {220} of the fcc-reverted austenite phases. The acquired data were analyzed using MTEX, a

free crystallographic texture analysis software, and the inverse pole figure (IPF) and orientation distribution function (ODF) were plotted.

Samples for microstructural characterization were prepared by grinding, mechanical polishing using diamond paste and final polishing with colloidal silica suspension. Secondary electron scanning electron microscopy micrographs were acquired before and after the in situ heat treatment from specimens that were etched with 3% nital. In addition, to track the martensite \rightarrow reverted austenite transformation during heat treatment, EBSD observations of the same sample regions were conducted. This consisted of repeated observation of the same specimen's area before and after heat treatment in a vacuum furnace. Here, the specimen was subjected to isothermal heat treatment at 570°C for 3 h in high vacuum (2×10^{-7} mbar) using a heating rate of $0.12^\circ\text{C s}^{-1}$. Notably, the heat treatment in vacuum did not cause oxidation of the sample's surface allowing the EBSD maps to be collected from the identical region prior to the heat treatment. Crystal orientation maps were obtained using FEI® Quanta FEG 450 and FEI® Quanta FEG 650 scanning electron microscopes (SEM) equipped with a HKL Oxford NordlysNano® camera utilizing the Aztec acquisition software. The acquired EBSD data were processed and plotted using Oxford Instruments HKL Channel 5 software.

RESULTS AND DISCUSSION

Prior to the in situ heat treatment, the microstructure of the steel consists of martensite packet boundaries and martensite lath boundaries confined in prior austenite grain boundaries depicted as PAGB (Fig. 1a). No second-phase precipitates were identified in this condition. After the in situ heat treatment, thin second-phase layers were generated along both the martensite packet boundaries and martensite lath boundaries and partially also at the prior austenite grain boundaries (Fig. 1b). The average thickness of the second-phase layers was measured in the range 45–75 nm.

Figure 2 shows a time-resolved color map of diffracted data in the 2θ range of 28° – 43° acquired during isothermal heat treatment at 570°C . In this figure, the intensity of diffraction patterns is represented by the change in color between red (highest intensity) and dark blue (lowest intensity). Prior to the heat treatment, two diffraction peaks attributed to the $(110)_\alpha$ and $(200)_\alpha$ crystallographic planes were identified from the map. With increasing heat treatment time, one can see an additional $(111)_\gamma$ peak after ~ 300 s of the heat treatment and then an increase of peak intensity for the $(111)_\gamma$, $(200)_\gamma$ and $(220)_\gamma$ crystallographic planes. Simultaneously, there was a reduction of the intensity of the $(110)_\alpha$ and $(200)_\alpha$ diffraction peaks of martensite with progressing time. The reduction of martensitic peaks and appearance of new austenitic peaks with

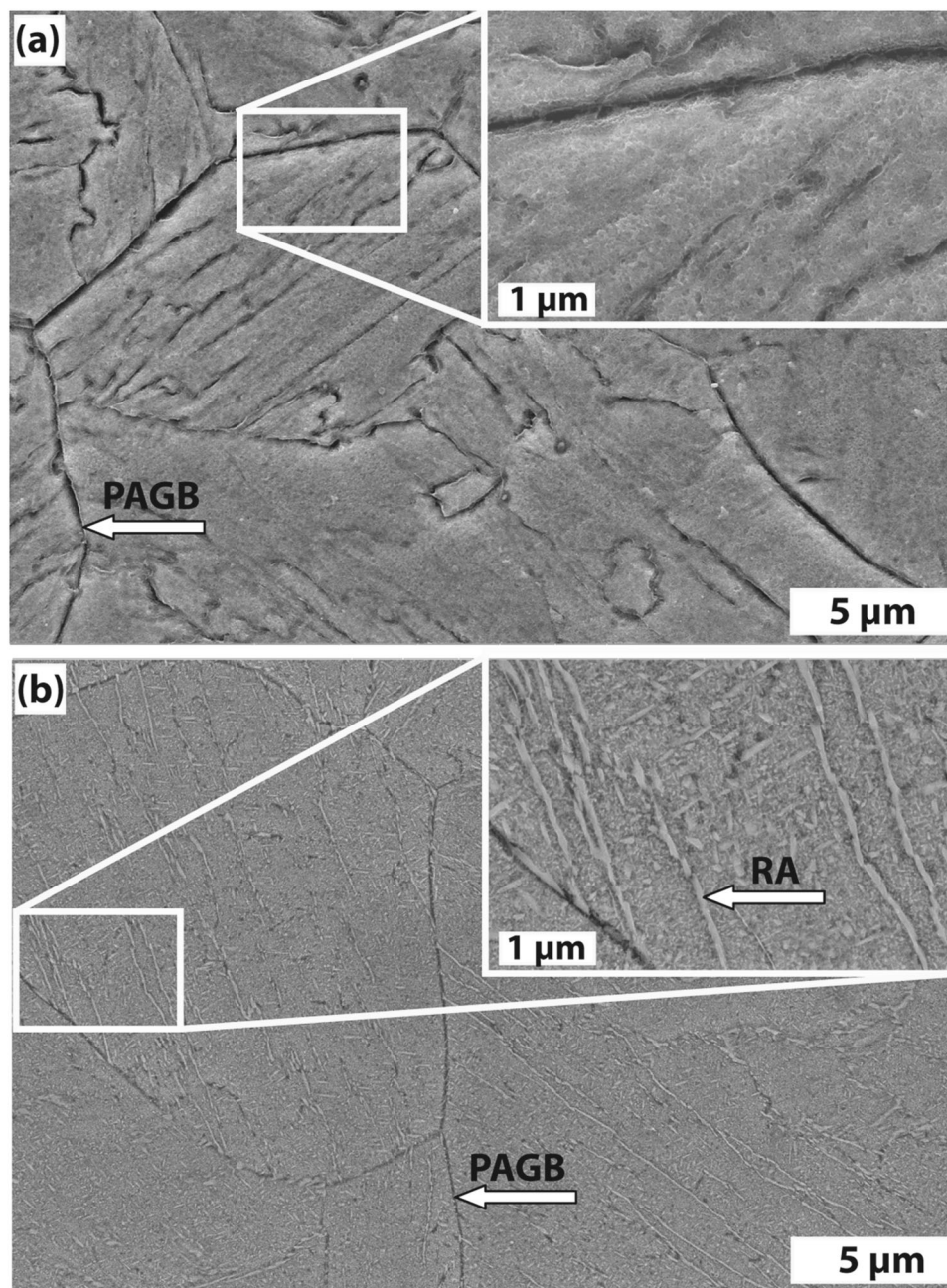


Fig. 1. Secondary electron micrographs of samples before (a) and after (b) in situ heat treatment. The PAGB depicts the prior austenite grain boundaries and RA reverted austenite.

progressing heat treatment time can be attributed to martensite \rightarrow reverted austenite transformation. The reverted austenite is known to form during diffusional decomposition of the matrix and/or precipitates.⁵⁶

An example of Rietveld refined synchrotron XRD patterns for the solution annealed and heat treated at 570°C/3 h sample is given in Fig. S1a-b. Figure S1a shows that the solution annealing heat treatment at 840°C for 1 h followed by cooling in air led to a complete austenite \rightarrow martensite transformation. The diffraction peaks fit well with the *I4*

space group. Because of the tetragonal distortion as evidenced by Nunes et al.⁵⁷ in 18 wt.% Ni grade 350 maraging steel. The calculation of the *c/a* ratio results in 1.00449. Such lattice distortion can induce localized strain fields because of the specific volume changes, which can provide additional driving force for the phase transformation.

Figure S1b shows the diffraction pattern recorded after isothermal heat treatment at 570°C for 3 h. Both martensite and austenite were identified from this diffractogram. The austenitic phase fits well with the *Fm* - *3 m* space group. The lattice

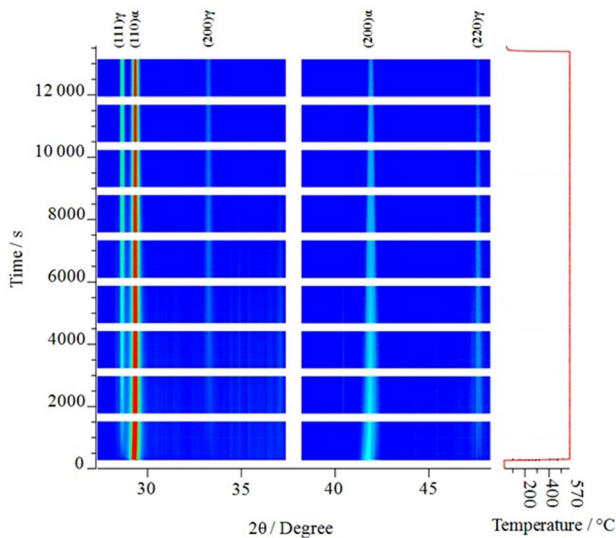


Fig. 2. Time-resolved color map of diffraction patterns collected between partial and complete scans during isothermal heat treatment at 570°C on the XTMS synchrotron line using a heating rate of 15°C s⁻¹. The intensity of diffraction patterns is represented by the change in color between red (highest intensity) and dark blue (lowest intensity). Extra time (horizontal white strips between blue-colored scans) was required to acquire complete scans, and this was approximately 270 s for each scan.

parameters for martensite and austenite were determined by the Rietveld method as $a = 2.904$ Å, $c = 2.892$ Å and $a = 3.635$ Å, respectively. No diffraction peaks corresponding to precipitates were identified. Sha et al.⁵ reported that the volume fraction of precipitates in 18 wt.% Ni grade 300 maraging steels is around 4 vol.%.

Figure 3a and b presents the evolution of lattice parameters in addition to the volume of the unit cell for both martensite and austenite as a function of aging time. Since the formation of both austenite and precipitates is a diffusion-controlled process, one might expect that lattice parameters of the phases present would change with progressing aging time. Figure 3a indeed confirms that diffusion takes place, since both the a and c lattice parameters of martensite increased in the early stage of aging and then were followed by a slight decrease until the end of the heat treatment. This suggests that there is a local enrichment and/or segregation of the alloying elements in the matrix during the isothermal aging process. Habiby et al.⁵⁸ reported a reduction in the lattice parameter of the martensite phase in 18 wt.% Ni grade 350 maraging steel when the material was aged at 400°C and then at 650°C. This reduction could be attributed to the depletion of alloying elements in the matrix due to precipitation of the intermetallic compounds and reversion of the austenite. These changes in lattice parameters are a consequence of diffusion of the alloying elements, mainly nickel, which stabilizes the austenitic phase.²⁶ In addition, Fig. 3 shows that the diffusion does not eliminate the tetragonal distortion from the cubic symmetry in the martensite.

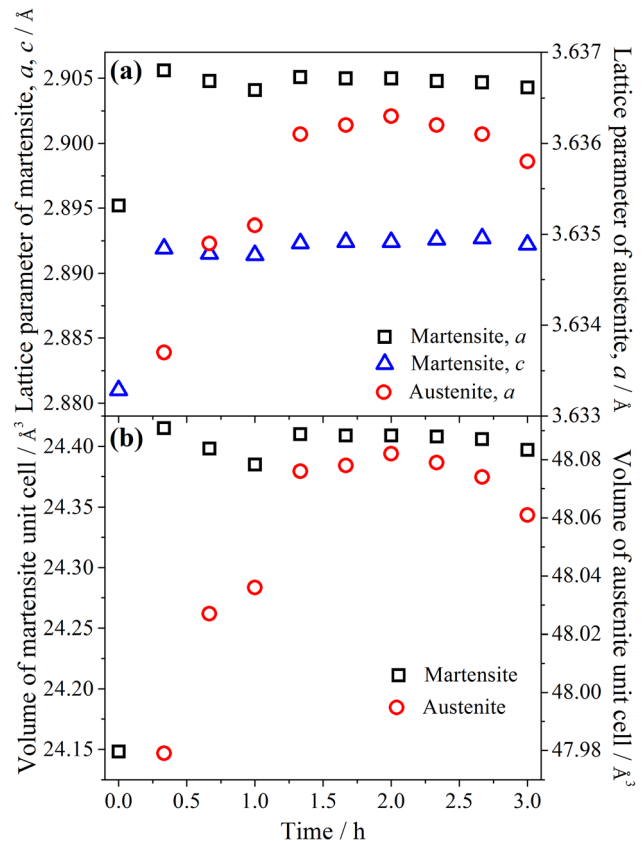


Fig. 3. Change of the lattice parameter (a) and volume of the unit cell (b) of martensite and austenite during isothermal heat treatment on the XTMS line at 570°C using a heating rate of 15°C s⁻¹.

This is in good agreement with results reported by Nunes et al.⁵⁷ in 18 wt.% Ni grade 350 maraging steel.

Figure 3b shows that during heat treatment, the volume of the reverted austenite unit cell increased up to 1 h of heat treatment and then remained nearly constant. The volume of reverted austenite unit cells can be associated with diffusion processes where redistribution of alloying elements between phases takes place.⁵⁷ A substitutional alloying element such as nickel (Ni) acts to stabilize the austenite along different types of interfaces including prior austenite grain boundaries, martensite packet, blocks and lath boundaries.⁷ In addition, interstitial alloying elements such as carbon (C) and nitrogen (N) may quickly partition under intercritical annealing or tempering treatments.^{59,60} Both contribute to the nucleation and growth of reverted austenite; however, due to differences in terms of atomic mobility, contributions are likely to occur at different times. As carbon and nitrogen diffuse rapidly in the matrix, they will initially contribute to nucleation of austenite grains. With the advance of the aging process, the segregation of substitutional alloying elements takes place. The Ni content is responsible for increasing both the volume unit cell and volume fraction of reverted austenite. This explains the apparent stabilization of the lattice

parameter of austenite at 3.636 Å and the volume unit cell of 48.08 Å. The small drop in lattice parameters observed at 3-h aging treatment may be attributed to atomic rearrangement within the austenite crystal.

Prior to the heat treatment, the volume of the martensite unit cell was determined to be 24.15 Å³. After 0.33 h of aging at 570°C, a value of approximately 24.4 Å³ was reached. The main contribution to this increase in the volume of the martensite unit cell can be primarily attributed to the thermal expansion of the martensitic matrix when reaching the aging temperature and to a smaller extent to the diffusion process. The volume of the martensite unit cell remained nearly constant for the rest of the heat treatment, indicating that the depletion of alloying elements in the matrix does not affect the volume of the martensite unit cell.

Figure 4 displays the volume fraction of reverted austenite *versus* aging time for an aging temperature of 570°C. In Fig. 4, the filled square points were acquired at room temperature, while the open square points were recorded during in situ isothermal heat treatment. As can be seen in this figure, after solution annealing (at the start of the in situ heat treatment at time 0 h), no retained austenite was present or its amount was below the detection limit of the XRD technique. However, we could detect ~ 5 vol.% austenite fraction at the early stage ~ 20 min of isothermal aging at 570°C. Aging for up to 3 h leads to a progressive increase of the volume fraction of reverted austenite. The determined volume fraction of reverted austenite after 3 h of aging treatment was 25.8% and after cooling to room temperature was 26.1%. The gradual reversion of martensite to austenite is an indication of a diffusion-controlled transformation process. This

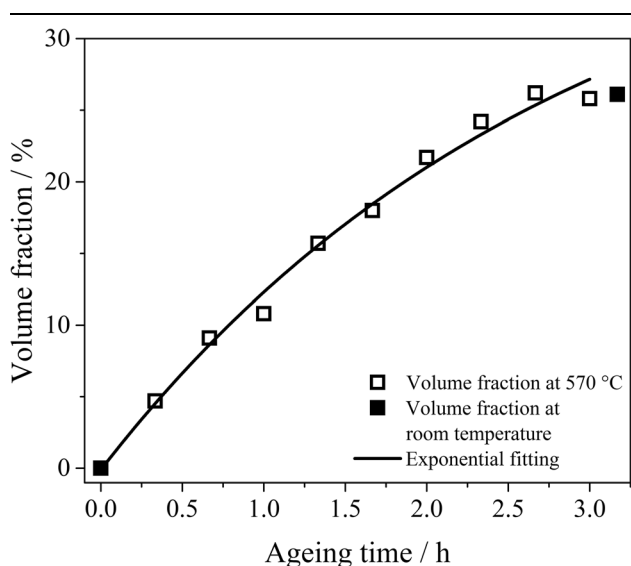


Fig. 4. Kinetics of reverted austenite formation during isothermal heat treatment on the XTMS line at 570°C using a heating rate of 15°C s⁻¹.

behavior is consistent with experimental data reported in the literature concerning the partitioning of austenite stabilization elements to the martensite lath boundary,^{8,61} which provide favorable conditions for the nucleation and growth of austenite. The nucleation and growth of the reversion of austenite in grade 300 maraging steel was described using the following equation²³

$$\gamma(t) = \gamma_{\max}(1 - e^{bt}) \quad (2)$$

where $\gamma(t)$ is the volume fraction of reverted austenite, γ_{\max} is the maximum volume fraction of the austenite transformed in this temperature, b is the negative exponent of time, and finally t is the aging time in hours. The exponential formula described in Eq. 1 correctly fits the experimental data for reversion of austenite as a function of aging time reported in Fig. 4, yielding values of $\gamma_{\max} = 41.68 \pm 6.30$ and $b = -0.35 \pm 0.08 \text{ h}^{-1}$, with correlation coefficient ~ 0.989 . The γ_{\max} obtained by the exponential fitting using Eq. 1 was approximately twice the one observed in Fig. 4. However, the aging time employed in this study was not enough to reach the maximum of austenite transformed, which can be reached only after prolonged aging times.^{22,23} In this work, after isothermal treatment was completed, the volume fraction of austenite remained constant during cooling to room temperature, indicating its thermal stability (Fig. 4).

The chemical composition of the steel studied was imported into the Thermo-Calc[®] software package with the TCFE6 database, and the equilibrium phase diagram was computed. The calculated equilibrium phase diagram indicated that the Ni₃Ti, Fe₇Mo₆ (μ -phase), austenite and martensite matrix were the stable phases at 570°C. However, no quantitative information could be obtained from the phase diagram. Therefore, Thermo-Calc[®] simulation of the phase fraction evolution during aging at equilibrium conditions was conducted, and the results are presented in Fig. S1 (see supplementary data file). The phase fraction of austenite increases rapidly after an aging temperature of 500°C until it reaches complete transformation at approximately 675°C. Ni₃Ti, Fe₇Mo₆ (μ -phase) and martensite tend to decrease their phase fraction above 500°C. The calculated phase fractions of Ni₃Ti, Fe₇Mo₆, martensite and austenite are approximately 3.1, 4.9, 45.7 and 46.3 vol.% at 570°C, respectively. The values of the volume fraction predicted at the equilibrium condition for both precipitates and austenite are in good agreement with experimental results reported by Sha et al.⁵ in grade 300 maraging steel aged at 510°C for 128 h.

In addition, supplementary Table SI presents the equilibrium chemical composition for all expected phases at 570°C determined by thermodynamic simulation. As can be seen in this table, the austenite phase has a high Ni content, which suggests that the austenite reversion reaction

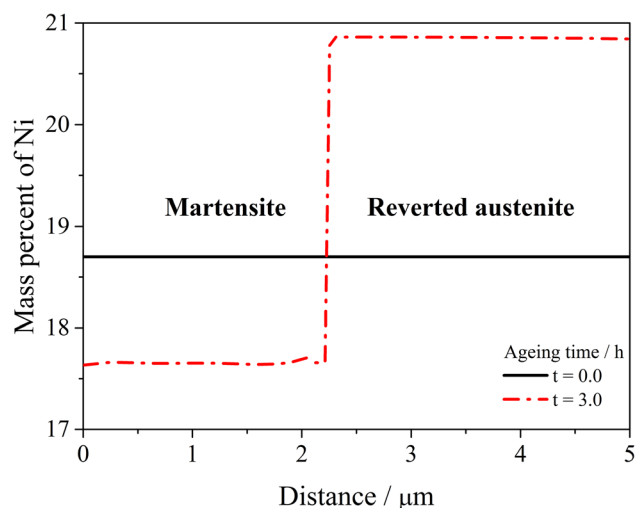


Fig. 5. Thermo-Calc[®] calculation of the Ni distribution at the martensite/austenite interface.

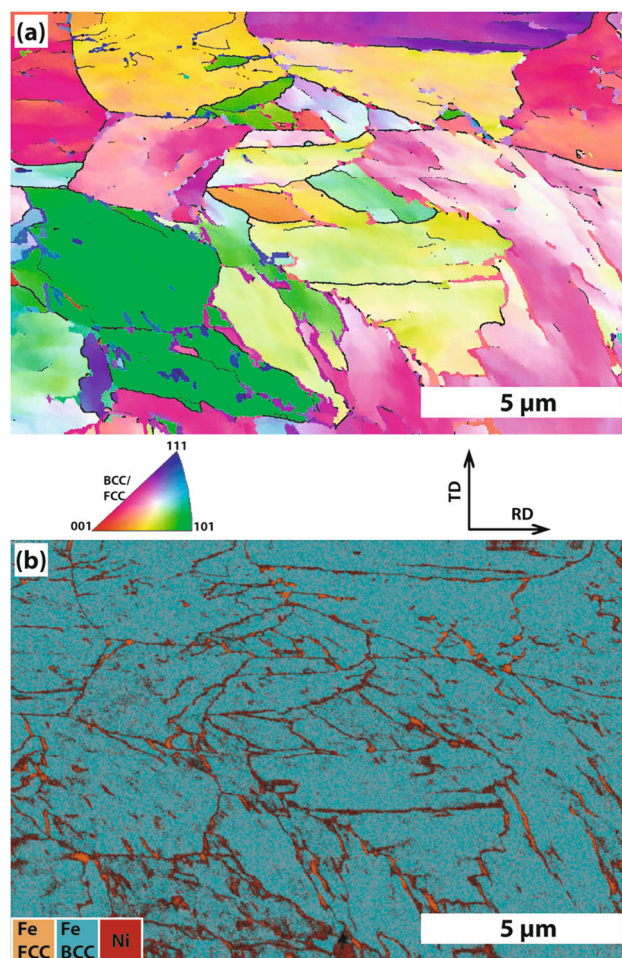


Fig. 6. (a) Inverse pole figure EBSD map and (b) composite map consisting of an EBSD phase map in conjunction with an energy-dispersive x-ray spectroscopy (EDS) map revealing segregation of Ni in reverted austenite.

occurs in Ni-enriched regions. Studies conducted in martensitic steels showed that Ni partitioning at the phase boundaries takes place.^{7,8} The compositional changes at the phase boundaries were explained by the large difference in diffusivity between martensite and austenite.⁸ Furthermore, the calculation of Ni diffusivity across the martensite/austenite interface was simulated using the Thermo-Calc[®] software, and the results of calculation are presented in Fig. 5. After 3 h of aging the reverted austenite phase was enriched with Ni. It is well known that Ni acts as austenite stabilizer element. The change in Ni content at the martensite-austenite interface and boundary motion towards martensite can explain the reverted austenite growth. Compositional inhomogeneities in the front of the martensite-austenite interface result in local segregation of Ni, which can promote growth of reverted austenite by a retention process. Under adequate aging time and temperature, an austenite stabilizer element such as Ni will segregate along the martensite grain boundaries and lath/lath interfaces, forming nickel-rich and nickel-depleted regions, which will promote the martensite-to-austenite reversion.

The XRD macrotexture analysis revealed that the [001] IPF (sample direction) presented a dominance of {111} and {101} crystallographic planes parallel to the normal direction in reverted austenite and martensite, respectively; see supplementary Fig. S2. Constant ODF was calculated and presented using a discrete set of crystal lattice orientation distributions. A weak texture was found in fcc-reverted austenite with maximum intensity of about 3.55 in gamma fiber {111}//ND) at (111)[-1-12] texture component. In contrast, a preferred texture parallel to {110} normal direction with maximum intensity of about 4.83 was found at (110)¹⁻¹¹ and (110)²⁻²¹ components.

The EBSD analysis confirmed that in the sample subjected to heat treatment at 570°C for 3 h, both martensite and reverted austenite phases are present (Fig. 6a and b). The corresponding energy-dispersive x-ray spectroscopy (EDS) map for element Ni combined with EBSD phase map revealed that a segregation of this element occurs in the reverted austenite grains (Fig. 6b). Our observation is also consistent with findings reported by other authors.^{7,8}

The reverted austenite forms at martensite lath boundaries and the Ni-content was found to be 20.3 wt.%. In contrast, the Ni content in the adjacent matrix was measured as 17.7 wt.%. The partitioning at interfaces in these classes of steels is commonly accompanied by reverse martensite-to-austenite transformation. Mun et al.⁵⁰ analyzed austenite reversion in Fe-8Mn-7Ni (wt.%) steel and observed that alloying elements including Mn and Ni were not segregated in the as-quenched condition. The segregation to martensite grain boundaries took place after annealing heat treatment at 450°C. Indeed, our EBSD analysis confirmed that the

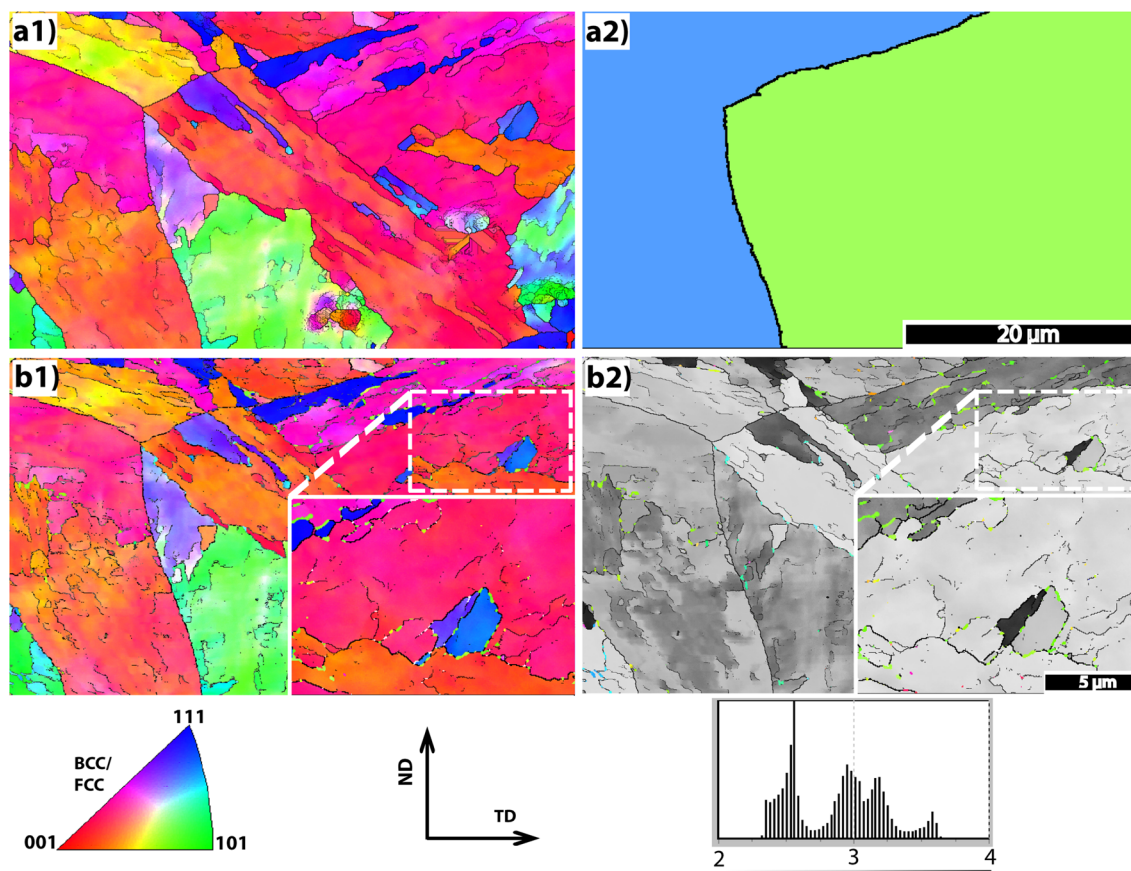


Fig. 7. EBSD inverse pole figure (IPF) maps of (a1) solution-treated material showing single-phase martensitic matrix; (a2) calculated prior austenite grains from orientations shown in (a1). The high- and low-angle grain boundaries are depicted with thick and thin black lines, respectively. IPF map of material heat treated at 570°C for 3 h using heating rate of 0.12°C s⁻¹ in vacuum revealing the martensitic matrix with reverted austenite formed at the grain and sub-grain boundaries (b1). Corresponding Taylor factor map combined with IPF map for fcc phase showing the formation of reverted austenite at the grain and sub-grain boundaries with high Taylor factor values (b2). A higher magnification view is shown in the inset micrographs. The scale bar for all large maps and all inset micrographs is 20 μm and 5 μm, respectively. Corresponding legends are shown below the maps.

second-phase layers are fcc austenite (Fig. 5a and b). Therefore, the Ni enrichment at newly formed α/γ interfaces led to the austenite layers growing to lath-like reverted austenite, which is consistent with Refs.^{7,48} Since partitioning of the matrix into solute-rich and solute-depleted regions occurs, the formation of reverted austenite is a diffusion-controlled process.

Figure 7a1 shows an inverse pole figure EBSD map of solution-treated material. The high-angle grain boundaries (defined as misorientation > 15°) and low-angle grain boundaries (with misorientation < 2°) are depicted with thick and thin black lines, respectively. The map shows a single-phase martensitic matrix. The martensite comprises a lamellar structure and forms units of packets. Figure 7a2 shows the prior austenite grains calculated experimentally from the orientation obtained in Fig. 7a1 using the ARPGE software. Two prior austenite grains were determined in the map with following Euler angles $\varphi_1, \Phi, \varphi_2 = 112.5^\circ, 108.9^\circ, 142.9^\circ$ and $89.7^\circ, 31.2^\circ, 102.9^\circ$ for the left and right grain, respectively. In the heat-treated sample at

570°C for 3 h in a vacuum chamber, the formation of reverted austenite with average grain size of 0.5 μm could be seen as presented in Fig. 7b1 and b2. Notably, the heat treatment in vacuum did not cause oxidation of the sample's surface, and therefore no further metallographic preparation was required prior to the EBSD examination. An elimination of metallographic preparation after the heat treatment is important because deformation-induced reverted austenite → martensite is commonly reported.^{18,33,34} The EBSD maps show that austenite precipitates mainly along the martensite lath boundaries and few grains were observed to precipitate at prior austenite grain boundaries.

In addition, the Taylor map in Fig. 7b2 revealed that the majority of reverted austenite grains nucleated at grains with higher Taylor factor values. The different Taylor factor values in individual grains can be associated with shear strains generated during austenite → martensite transformation, which took place during cooling from the solution annealing temperature. Since there was no recrystallisation during the heat treatment, the

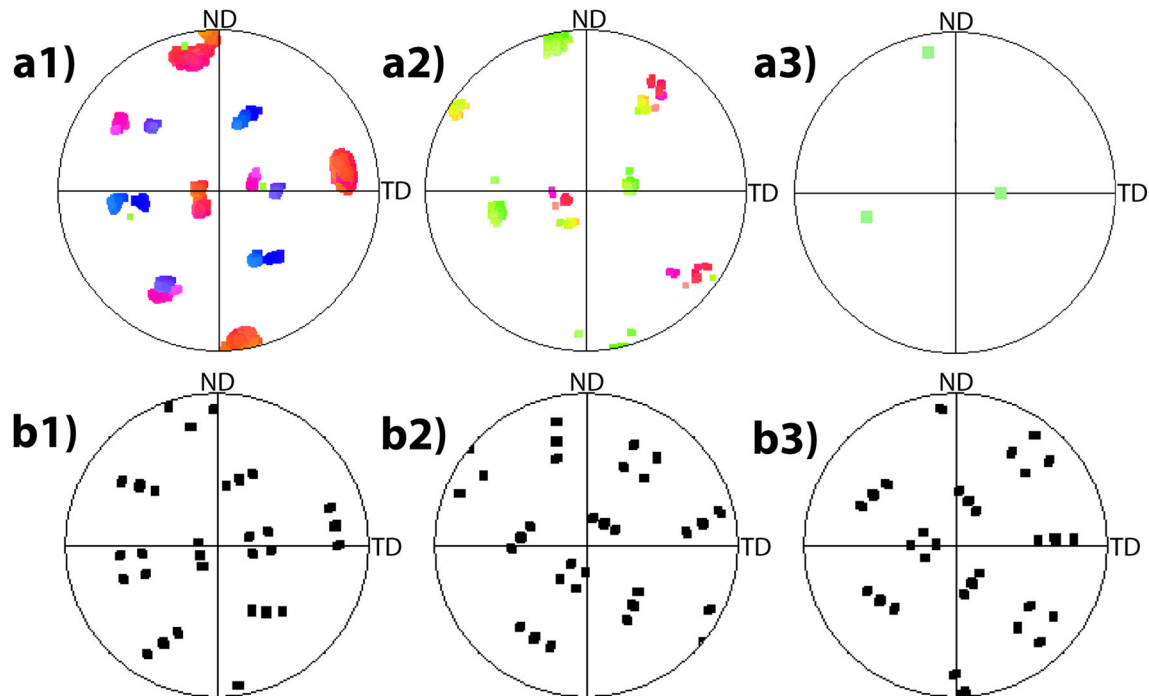


Fig. 8. Experimentally obtained and calculated $\{100\}$ pole figures for orientations in the inset map shown in Fig. 7 (b1) for martensite and reverted austenite. (a1) Experimentally determined bcc pole figure. (a2) Experimentally obtained $\{100\}$ fcc pole figure. (a3) Calculated pole figure of prior austenite considering experimentally obtained orientations in (a1) revealing good coincidence with some poles for reverted austenite displayed in (a2). (b) Calculated $\{100\}$ bcc pole figures for green (b1), yellow (b2) and red (b3) orientations shown in (a2) showing good agreements with some poles displayed in (a1).

Taylor factor values remained constant. A higher Taylor factor indicates higher stored energy in the grains, which can provide an additional driving force for nucleation of the new phase.^{62–64} An additional reason for austenite precipitation along martensitic lath boundaries is partitioning of austenite stabilization elements to the martensite boundary.^{8,61}

In maraging steels, in the initial stage of the martensite-to-austenite reversion process first carbon partitioning takes place.⁷ Speer et al.⁶⁵ claimed that in TRIP steel heat treatment at $400^{\circ}\text{C} < 1$ s was necessary for carbon partitioning between martensite and austenite. Even at the very low carbon content present in the investigated steel, we found tetragonal distortion from the cubic symmetry in the martensite. This contributes to the enhancement of the elastic strain of the crystal lattice, in particular at grain boundaries where the diffusivity of carbon is higher because of the lattice distortion. In this manner, the accumulated carbon in front of the martensite boundary provides a high local driving force for austenite nucleation. Indeed, the EBSD analysis revealed that austenite tends to nucleate at martensite grain boundaries with higher Taylor factor values. Higher Taylor factor values calculated by averaging the stress over all possible slip planes provide a measure of an orientation-dependent stored energy in grains. In the later stages of the in situ heat treatment, the solute element diffusion controls the transformation

kinetics.⁸ It is also known that slip is more restricted in grains with a high Taylor factor, resulting in the formation of a tangled structure with lattice rotations, which increase the grain boundary segregation of alloying elements (such as Ni), thereby accelerating austenite reversion.⁶⁶ Hence, the grain boundary segregation of alloying elements is required to form reversed austenite, and elastic strain relaxation stabilizes the formation of austenite.⁷ Our results revealed that the newly formed reverted austenite did not exhibit lattice distortion and its formation therefore contributes to the minimization of the total free energy of the system.

The inset micrograph of Fig. 7b2 shows that different orientations of reverted austenite are present. These have a common habit plane with the prior austenite grain, and these are in a twin relationship to each other. The volume fraction of reverted austenite determined by EBSD was 2 vol.%, which is different from that determined by the XRD analysis of the in situ heat-treated specimen. This difference may be caused by the different heating rates ($0.12^{\circ}\text{C s}^{-1}$ versus $15^{\circ}\text{C s}^{-1}$) used. Nevertheless, the nucleation sites of reverted austenite are considered independent of the heating rate applied.

Figure 8 shows experimentally obtained and calculated $\{100\}$ pole figures derived from orientations presented in the inset map of Fig. 7b1 for both martensite and reverted austenite. Figure 8a1

shows the experimentally determined pole figure of martensite, whereas Fig. 8b2 presents an experimentally obtained pole figure of reverted austenite. Figure 8b3 displays the calculated pole figure of prior austenite considering the experimentally obtained bcc orientations shown in a1 using ARPGE software. A comparison of the calculated pole figure of prior austenite with the experimentally obtained pole figure of reverted austenite shown in Fig. 8a2 revealed that within one prior austenite grain most of the reverted austenite maintains the same crystallographic orientation. Some reverted austenite grains showed a twin-related misorientation in relation to the prior austenite. This is in good agreement with the work of Nakada et al.³¹ who reported a twin relationship between reverted and prior austenite. The orientation relationship between reverted austenite and martensite was close to the Kurdjumov–Sachs type, which is $(111)_\gamma // (110)_{\alpha'}$, $[110]_\gamma // [111]_{\alpha'}$. The obtained sets of Euler angles for green, yellow and red grains of reverted austenite shown in the inset micrograph in Fig. 7b1 were imported into the program developed by Kundu,⁶⁷ which is based on the phenomenologic martensite transformation crystallography. Then, the bcc orientation was calculated using the Patel-Cohen model considering 24 variants. Figure 8b1, b2, and b3 shows the results of this calculation. Some of the poles in the pole figure match those obtained experimentally in Fig. 8a1 well. Since fewer poles were present in the experimentally obtained pole figure compared to the theoretical one, variant selection is present. The variant selection can be attributed to internal stresses introduced by martensitic transformation.³¹ The orientation relationships minimize the strain energy of the phase transformation by reducing the crystallographic mismatch between phases.

CONCLUSION

The kinetics of reverted austenite formation was followed in situ using synchrotron x-ray diffraction in 18 wt.% Ni grade 300 maraging steel subjected to isothermal heat treatment at 570°C for durations up to 3 h. From the work conducted, we can draw following conclusions.

A progressive increase in the volume fraction of reverted austenite was observed during the heat treatment. The reversion of austenite was well fitted by exponential fitting. Fairly good agreement between the experimental and calculated degree of transformation was found. Preferential nucleation sites for reverted austenite were found to be martensitic lath boundaries, in particular those with high Taylor factor values. The martensite unit cell was observed to have a distortion from the cubic symmetry. This lattice distortion can induce localized strain fields due to specific volume changes, which could provide an additional driving force for

the austenite reversion. The reverted austenite maintains an orientation relationship with the prior austenite; however, variant selection can take place.

ACKNOWLEDGEMENTS

Experimental support of Mr. F.E. Montoro, Dr. O.R. Bagnato and Dr. A.L. Gobbi (Projects SEM 21795 and LMF 20869) at Brazilian Nanotechnology National Laboratory-LNNano is acknowledged. Microstructural characterization was performed at the Analytical Centre-UFC/CT-INFRA/MCTI-SIS-NANO/Pró-Equipamentos CAPES and LNNano. The authors acknowledge the Brazilian Synchrotron Light Laboratory-LNLS for the use of the XTMS installation at the XRD-1 beamline. This study used the resources of the Brazilian Synchrotron Light Laboratory (Project 20170162), an open national facility operated by the Brazilian Center for Research in Energy and Materials for the Brazilian Ministry for Science, Technology, Innovations and Communications. This work was financed in part by the Coordenação de Aperfeiçoamento de Pessoal de Nível Superior-Brasil (CAPES)-Finance Code 001 and Conselho Nacional de Desenvolvimento Científico e Tecnológico-CNPq.

ELECTRONIC SUPPLEMENTARY MATERIAL

The online version of this article (<https://doi.org/10.1007/s11837-020-04254-w>) contains supplementary material, which is available to authorized users.

REFERENCES

1. V.K. Vasudevan, S.J. Kim, and C.M. Wayman, *Metall. Trans. A* 21, 2655 (1990).
2. W. Sha, *Scr. Mater.* 42, 549 (2000).
3. S.S.M. Tavares, H.F.G. Abreu, J.M. Neto, M.R. Da Silva, and I. Popa, *J. Alloys Compd.* 358, 152 (2003).
4. W. Sha, A. Cerezo, and G.D.W. Smith, *Metall. Mater. Trans. A* 24, 1241 (1993).
5. W. Sha, A. Cerezo, and G.D.W. Smith, *Metall. Mater. Trans. A* 24, 1221 (1993).
6. U.K. Viswanathan, G.K. Dey, and M.K. Asundi, *Metall. Trans. A* 24, 2429 (1993).
7. D. Raabe, S. Sandlöbes, J. Millán, D. Ponge, H. Assadi, M. Herbig, and P.-P. Choi, *Acta Mater.* 61, 6132 (2013).
8. O. Dmitrieva, D. Ponge, G. Inden, J. Millán, P. Choi, J. Sietsma, and D. Raabe, *Acta Mater.* 59, 364 (2011).
9. M. Farooque, H. Ayub, A.U. Haq, and A.Q. Khan, *J. Mater. Sci.* 33, 2927 (1998).
10. D. Raabe, M. Herbig, S. Sandlöbes, Y. Li, D. Tytko, M. Kuzmina, D. Ponge, and P.-P. Choi, *Curr. Opin. Solid State Mater. Sci.* 18, 253 (2014).
11. M. Belde, H. Springer, G. Inden, and D. Raabe, *Acta Mater.* 86, 1 (2015).
12. J. Mitra, G.K. Dey, D. Sen, A.K. Patra, S. Mazumder, and P.K. De, *Scr. Mater.* 51, 34953 (2004).

13. R. Schnitzer, G.A. Zickler, E. Lach, H. Clemens, S. Zinner, T. Lippmann, and H. Leitner, *Mater. Sci. Eng., A* 527, 2065 (2010).
14. P.W. Hochanadel, G.R. Edwards, C.V. Robino, and M.J. Cieslak, *Metall. Mater. Trans. A* 25, 789 (1994).
15. J.-M. Cloué, B. Viguier, and E. Andrieu, *Metall. Mater. Trans. A* 36, 2633 (2005).
16. J. Suryawanshi, K.G. Prashanth, and U. Ramamurty, *J. Alloys Compd.* 725, 355 (2017).
17. E.V. Pereloma, A. Shekhter, M.K. Miller, and S.P. Ringer, *Acta Mater.* 52, 5589 (2004).
18. M.M. Wang, C.C. Tasan, D. Ponge, A. Kostka, and D. Raabe, *Acta Mater.* 79, 268 (2014).
19. X.C. Xiong, B. Chen, M.X. Huang, J.F. Wang, and L. Wang, *Scr. Mater.* 68, 321 (2013).
20. S. Lee, S.-J. Lee, and B.C. De Cooman, *Scr. Mater.* 65, 225 (2011).
21. C.A. Pampillo and H.W. Paxton, *Metall. Trans.* 3, 2895 (1972).
22. R. Schnitzer, R. Radis, M. Nöhrer, M. Schober, R. Hochfellner, S. Zinner, E. Povoden-Karadeniz, E. Kozeschnik, and H. Leitner, *Mater. Chem. Phys.* 122, 138 (2010).
23. J.M. Pardal, S.S.M. Tavares, V.F. Terra, M.R. da Silva, and D.R. dos Santos, *J. Alloys Compd.* 393, 109 (2005).
24. F. Habiby, T.N. Siddiqui, S.H. Khan, and A.Q. Khan, *NDT E Int.* 25, 145 (1992).
25. S.H. Khan, A.N. Khan, F. Ali, M.A. Iqbal, and H.K. Shukaib, *J. Alloys Compd.* 474, 254 (2009).
26. X. Li and Z. Yin, *Mater. Lett.* 24, 239 (1995).
27. G.M.C. Güiza and C.A.S. Oliveira, *Mater. Sci. Eng., A* 655, 142 (2016).
28. G.C.S. Nunes, P.W.C. Sarvezuk, T.J.B. Alves, V. Biondo, F.F. Ivashita, and A. Paesano Jr, *J. Magn. Magn. Mater.* 421, 457 (2017).
29. Y.Y. Song, X.Y. Li, L.J. Rong, D.H. Ping, F.X. Yin, and Y.Y. Li, *Mater. Lett.* 64, 1411 (2010).
30. N.F. Viana, S. Nunes, and H.F.G. de Abreu, *J. Mater. Res. Technol.* 2, 298 (2013).
31. N. Nakada, T. Tsuchiyama, S. Takaki, and S. Hashizume, *ISIJ Int.* 47, 1527 (2007).
32. A. Markfeld and A. Rosen, *Mater. Sci. Eng.* 46, 151 (1980).
33. G.A. Zickler, R. Schnitzer, R. Hochfellner, T. Lippmann, S. Zinner, and H. Leitner, *Int. J. Mater. Res.* 100, 1566 (2009).
34. Y. Katz, H. Mathias, and S. Nadv, *Metall. Trans. A* 14, 801 (1983).
35. J.M. Pardal, S.S.M. Tavares, M.P.C. Fonseca, H.F.G. Abreu, and J.J.M. Silva, *J. Mater. Sci.* 41, 2301 (2006).
36. N. Jia, Z.H. Cong, X. Sun, S. Cheng, Z.H. Nie, Y. Ren, P.K. Liaw, and Y.D. Wang, *Acta Mater.* 57, 3965 (2009).
37. R. Blondé, E. Jimenez-Melero, L. Zhao, J.P. Wright, E. Brück, S. Van der Zwaag, and N.H. Van Dijk, *Acta Mater.* 60, 565 (2012).
38. P.J. Jacques, Q. Furnémont, F. Lani, T. Pardoën, and F. Delannay, *Acta Mater.* 55, 3681 (2007).
39. J. Mu, Z. Zhu, R. Su, Y. Wang, H. Zhang, and Y. Ren, *Acta Mater.* 61, 5008 (2013).
40. J. Zhang, S. Hao, D. Jiang, Y. Huan, L. Cui, Y. Liu, H. Yang, and Y. Ren, *Acta Mater.* 130, 297 (2017).
41. M. Wiessner, E. Gamsjäger, S. van der Zwaag, and P. Angerer, *Mater. Sci. Eng., A* 682, 117 (2017).
42. E. Eidenberger, M. Schober, E. Stergar, H. Leitner, P. Staron, and H. Clemens, *Metall. Mater. Trans. A* 41, 1230 (2010).
43. P. Staron, T. Fischer, T. Lippmann, A. Stark, S. Daneshpour, D. Schnubel, E. Uhlmann, R. Gerstenberger, B. Camin, and W. Reimers, *Adv. Eng. Mater.* 13, 658 (2011).
44. J.W. Elmer, T.A. Palmer, and E.D. Specht, *Metall. Mater. Trans. A* 38, 464 (2007).
45. S. Ackermann, S. Martin, M.R. Schwarz, C. Schimpf, D. Kulawinski, C. Lathe, S. Henkel, D. Rafaja, H. Biermann, and A. Weidner, *Metall. Mater. Trans. A* 47, 95 (2016).
46. S.S. Babu, E.D. Specht, S.A. David, E. Karapetrova, P. Zschack, M. Peet, and H. Bhadeshia, *Metall. Mater. Trans. A* 36, 3281 (2005).
47. J. Epp, T. Hirsch, and C. Curfs, *Metall. Mater. Trans. A* 43, 2210 (2012).
48. F.F. Conde, J.D. Escobar, J.P. Oliveira, A.L. Jardini, W.W. Bose Filho, and J.A. Avila, *Addit. Manuf.* 29, 100804 (2019).
49. L. Yuan, D. Ponge, J. Wittig, P. Choi, J.A. Jiménez, and D. Raabe, *Acta Mater.* 60, 2790 (2012).
50. S.-H. Mun, M. Watanabe, D.B. Williams, X. Li, K.H. Oh, and H.-C. Lee, *Metall. Mater. Trans. A* 33, 1057 (2002).
51. H. Springer, M. Belde, and D. Raabe, *Mater. Sci. Eng., A* 582, 235 (2013).
52. H.M. Rietveld, *Acta Crystallogr.* 20, 508 (1966).
53. H. Rietveld, *J. Appl. Crystallogr.* 2, 65 (1969).
54. T. Roisnel and J. Rodriguez-Carvajal, *Mater. Sci. Forum* 378, 118 (1999).
55. R.J. Hill and C.J. Howard, *J. Appl. Crystallogr.* 20, 467 (1987).
56. S.S.M. Tavares, M.R. Da Silva, J.M. Neto, J.M. Pardal, M.P.C. Fonseca, and H.F.G. Abreu, *J. Alloys Compd.* 373, 304 (2004).
57. G.C.S. Nunes, P.W.C. Sarvezuk, V. Biondo, M.C. Blanco, M.V.S. Nunes, A.M.H. De Andrade, and A. Paesano, Jr, *J. Alloys Compd.* 646, 321 (2015).
58. F. Habiby, T.N. Siddiqui, H. Hussain, A.U. Haq, and A.Q. Khan, *J. Mater. Sci.* 31, 305 (1996).
59. O. Thuillier, F. Danoix, M. Gouné, and D. Blavette, *Scr. Mater.* 55, 1071 (2006).
60. D.V. Edmonds, K. He, F.C. Rizzo, B.C. De Cooman, D.K. Matlock, and J.G. Speer, *Mater. Sci. Eng., A* 438, 25 (2006).
61. E.I. Galindo-Nava, W.M. Rainforth, and P.E.J. Rivera-Diazdel-Castillo, *Acta Mater.* 117, 270 (2016).
62. J.M. Rosenberg and H.R. Piehler, *Metall. Trans.* 2, 257 (1971).
63. G.I. Taylor, *J. Inst. Met.* 62, 307 (1938).
64. P. Van Houtte, S. Li, M. Seefeldt, and L. Delannay, *Int. J. Plast.* 21, 589 (2005).
65. J.G. Speer, D.V. Edmonds, F.C. Rizzo, and D.K. Matlock, *Curr. Opin. Solid State Mater. Sci.* 8, 219 (2004).
66. F. Qian and W.M. Rainforth, *J. Mater. Sci.* 54, 6624 (2019).
67. S. Kundu, Transformation strain and crystallographic texture in steels, Ph.D. Thesis, University of Cambridge (2007).

Publisher's Note Springer Nature remains neutral with regard to jurisdictional claims in published maps and institutional affiliations.